Case Studies in Thermal Engineering 28 (2021) 101528

Contents lists available at ScienceDirect

Case Studies in Thermal Engineering

journal homepage: www.elsevier.com/locate/csite

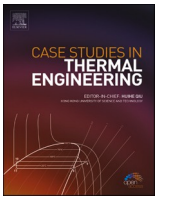

Direct numerical simulation of confined weak round fountains in homogeneous ambient

Liqiang Dong, Wenxian Lin *, Mehdi Khatamifar

College of Science & Engineering, James Cook University, Townsville, QLD, 4811, Australia

ARTICLE INFO

Keywords:
Filling box
Fountain
Wall fountain
Stratification
Direct numerical simulation

ABSTRACT

Fountains (negatively buoyant jets) are commonly used in numerous engineering applications, such as the natural ventilation in buildings and the smoke spread in compartment fires. In this study, the long-term behavior of weak round fountains in homogeneous ambient confined in a cylindrical container was analyzed using three-dimensional direct numerical simulation over a range of the Froude number (*Fr*), Reynolds number (Re), dimensionless radius of the container (λ), respectively. The confined weak round fountain behaves in the manner of a 'fountain filling box' flow, experiencing five development stages, *i.e.*, the formation of the fountain flow, the intrusion flow, the wall fountain, the reversed flow and the stratification. Three stages of the development of the bulk entrainment rate are identified and the dominant mechanisms involved are analyzed. $Fr = 1$ and 2 are identified as the approximate critical values to distinguish the behavior of the intrusion, wall fountain and stratification. $Re = 200$ is determined as the approximate critical value to distinguish the influence of Re. These are consistent with the existing results about the round fountains.

1. Introduction

Fountains (negatively buoyant jets), are widely involved in numerous natural and industrial settings [1]. When a dense jet is ejected upward into a lighter ambient fluid, a fountain is formed. Due to the negative buoyancy, the vertical velocity of the dense jet flow is gradually decreased until zero when the flow attains its maximum penetration height and the fountain flow subsequently falls back to form a downflow, which interacts with the upflow of the dense jet flow within the core of the fountain and the ambient fluid. The same flow is also found in the process where a light jet is discharged downward into a denser ambient fluid. The downflow fountain can produce strong secondary shear flows in the ambient after it impinges on the bottom floor. Without confinement, a radially outward spreading intrusion is resulted from the downflow after it impinges on the bottom floor. The intrusion behaves in a similar manner to a free-propagating radial gravity current as discussed by Chen [2], which may experience the 'wall-jet' (W-J) regime, the 'buoyancy-inertial' (B–I) regime, and finally the 'buoyancy-viscosity' (B-J) regime, in terms of the governing forces. Such free fountain cases are usually involved in large-scale environmental flows, *e.g.*, discharging the brine from desalination plants into the sea or the explosive volcanic eruptions [1]. However, in many applications of practical interest, a fountain usually occurs in a confined space, such as the natural ventilation and the reverse cycle air-conditioning systems in the building [3–5], smoke spread in compartment fires [6], and the leakage of hazardous gas in a limited space [1]. Inherently, the behavior of the confined fountain is different from that of a

* Corresponding author.
E-mail address: wenxian.lin@jcu.edu.au (W. Lin).

https://doi.org/10.1016/j.csite.2021.101528
Received 10 April 2021; Received in revised form 8 August 2021; Accepted 2 October 2021
Available online 4 October 2021

free fountain flow due to the confinement. When the confinement is not large, the intrusion will impinge with the vertical sidewall and move upwards along the wall to form a wall fountain. Since the flow remains denser than the ambient fluid, the wall fountain will then fall back after reaching its maximum penetration height, which will subsequently form a reversed flow moving toward the core region of the fountain flow ejected from the fountain source, interacting with the intrusion and the ambient fluid on the way. With the continuous ejection of the fountain fluid, a density stratification of fluid is then gradually formed in the confined space. Such a confined fountain flow was denoted as the 'fountain filling box model' by Baines, Turner & Campbell [7], which is a complementary model to the 'plume filling box model' proposed by Baines & Turner [8].

The behavior of a fountain in an unconfined homogeneous ambient fluid (termed 'free fountain'), is mainly governed by the Reynolds number Re and the Froude number *Fr*. Round fountains ejected from a round source, can be classified as very weak, weak, intermediate, forced, and highly forced in terms of *Fr* alone [1], or laminar, transitional and turbulent in terms of Re alone [9], although there is no definite explicit classification in terms of both *Fr* and Re. To date, extensive studies have been on free fountains, with earlier ones mainly on turbulent fountains in homogeneous ambient and more recent ones being extended to weak, laminar and transitional fountains in both homogeneous and stratified ambient. A good understanding of the behavior of free fountains has been obtained, mainly in terms of the fountain penetration height and the entrainment rate, as summarised in *e.g.*, Refs. [1,9–15]. However, the behavior of confined fountains is much less understood.

In the early study of the confined turbulent round fountain, Baines et al. [7] took into account of the entrainment, but the influence of the confinement extent was not addressed. A similar shortage also exists in the research to determine the entrainment rate of fountains by using plumes impinging with a density interface (see, *e.g.*, Refs. [16–18]). Shrinivas & Hunt [19] experimentally studied the influence of the confinement on the entrainment of fountain when buoyant fluid turbulently entrained across a density interface which separates two uniform layers within the confines of a box, in terms of the confinement parameter λ_i which is denoted as the ratio of the interfacial turbulence length scale to the depth of the upper layer. They noted that when λ_i is small, the entrainment is influenced by a weak secondary flow, following the scaling relation of $E_i \propto Fr_i^2$, where E_i and Fr_i are the dimensionless entrainment flux across the interface and the interfacial Froude number respectively, and when λ_i becomes large, a strong secondary flow formed significantly influences the entrainment, with the scaling relation of $E_i \propto Fr_i^3$. More recently, Debugne & Hunt [20] experimentally identified four flow regimes for the spanwise confined turbulent round fountains over $0.5 \leq Fr \leq 96$ and $2 < \lambda < 24$, where λ is the dimensionless radius of the container non-dimensionalized by the fountain source radius R_0. In their study, a 'confined' Froude number $Fr_c \equiv Fr(W/R_0)^{-5/4}$ was determined as the governing parameter to encompasses the confinement influence. Xue, Khodaparast & Stone [21] conducted a series of experiments to investigate the behavior of round fountains over $\mathrm{Re} < 500$ and $5 \leq Fr \leq 35$ in confined square tanks, and found that both the volume entrainment flux ratio and the fountain penetration height reach a local peak at an intermediate Reynolds number ($\mathrm{Re} \approx 200$). Additionally, the confinement effect was observed to enhance the horizontal mixing within the layer of the mixture formed at the top. Nevertheless, with only two square tanks of relatively large aspect ratios to provide weak confinement, no clear understanding of the confinement influence was obtained. The present paper is motivated to provide a better understanding of the long-term behavior of confined weak round fountains in homogeneous ambient.

The remainder of this paper is organized as follows. The details of the three-dimensional DNS runs and the mesh and time-step independence test results are briefly described in § 2. The DNS results are benchmarked in § 3 by comparing the numerical results produced by several representative DNS runs with the corresponding experimental results obtained with high-speed cameras and visualization experiments. In § 4, the evolution of the typical confined weak round fountain is described qualitatively with the DNS results, along with the qualitative discussions of the influence of *Fr*, Re and λ. A quantitative analysis is also presented in § 4 to quantify the influence of *Fr*, Re and λ on the characteristics of the transient behavior of confined weak round fountains, including the intrusion, wall fountain, stratification and bulk entrainment/dilution rate. Finally the conclusions are drawn in § 5.

2. Numerical methodology

The physical system under consideration is a vertical cylindrical container of radius R_c and height H, with a non-slip and insulated sidewall and an open top surface. An orifice of radius R_0 located on the bottom center is used as the round fountain source. The rest region of the bottom is rigid, non-slip and insulated. The container initially contains a quiescent homogeneous Newtonian fluid at the uniform temperature T_a. At $t = 0$, a dense jet at temperature T_0 ($T_0 < T_a$) is ejected upward into the container from the source at the uniform velocity W_0 and this discharge is maintained thereafter. For a three-dimensional round fountain in a confined homogeneous ambient fluid, the governing equations, *i.e.*, the three-dimensional incompressible Navier-Stokes equations and the temperature equation can be written in cylindrical coordinates (R, Φ, Z) as follows,

$$\frac{1}{R}\frac{\partial(RU_R)}{\partial R}+\frac{1}{R}\frac{\partial U_\Phi}{\partial \Phi}+\frac{\partial U_Z}{\partial Z}=0, \tag{1}$$

$$\frac{\partial U_R}{\partial t}+U_R\frac{\partial U_R}{\partial R}+\frac{U_\Phi}{R}\frac{\partial U_R}{\partial \Phi}-\frac{U_\Phi^2}{R}+U_Z\frac{\partial U_R}{\partial Z}=$$

$$-\frac{1}{\rho}\frac{\partial P}{\partial R}+\nu\left[\frac{1}{R}\frac{\partial}{\partial R}\left(R\frac{\partial U_R}{\partial R}\right)-\frac{U_R}{R^2}+\frac{1}{R^2}\frac{\partial^2 U_R}{\partial \Phi^2}-\frac{2}{R^2}\frac{\partial U_\Phi}{\partial \Phi}+\frac{\partial^2 U_R}{\partial Z^2}\right], \tag{2}$$

$$\frac{\partial U_\Phi}{\partial t}+U_R\frac{\partial U_\Phi}{\partial R}+\frac{U_\Phi}{R}\frac{\partial U_\Phi}{\partial \Phi}+\frac{U_R U_\Phi}{R}+U_Z\frac{\partial U_\Phi}{\partial Z}=$$

$$-\frac{1}{\rho}\frac{1}{R}\frac{\partial P}{\partial \Phi}+\nu\left[\frac{1}{R}\frac{\partial}{\partial R}\left(R\frac{\partial U_\Phi}{\partial R}\right)-\frac{U_\Phi}{R^2}+\frac{1}{R^2}\frac{\partial^2 U_\Phi}{\partial \Phi^2}-\frac{2}{R^2}\frac{\partial U_R}{\partial \Phi}+\frac{\partial^2 U_\Phi}{\partial Z^2}\right], \tag{3}$$

$$\frac{\partial U_Z}{\partial t}+U_R\frac{\partial U_Z}{\partial R}+\frac{U_\varphi}{R}\frac{\partial U_Z}{\partial \Phi}+U_Z\frac{\partial U_Z}{\partial Z}=$$

$$-\frac{1}{\rho}\frac{\partial P}{\partial Z}+\nu\left[\frac{1}{R}\frac{\partial}{\partial R}\left(R\frac{\partial U_Z}{\partial R}\right)+\frac{1}{R^2}\frac{\partial^2 U_Z}{\partial \Phi^2}+\frac{\partial^2 U_Z}{\partial Z^2}\right]+g\beta(T-T_0), \tag{4}$$

$$\frac{\partial T}{\partial t}+U_R\frac{\partial T}{\partial R}+\frac{U_\Phi}{R}\frac{\partial T}{\partial \Phi}+U_Z\frac{\partial T}{\partial Z}=\kappa\left[\frac{1}{R}\frac{\partial}{\partial R}\left(R\frac{\partial T}{\partial R}\right)+\frac{1}{R^2}\frac{\partial^2 T}{\partial \Phi^2}+\frac{\partial^2 T}{\partial Z^2}\right], \tag{5}$$

in which the dimensional quantities R, Z and Φ are the coordinates, U_R, U_Z and U_φ are velocity components in the R, Z and Φ directions, T is temperature, t is time, g is the acceleration due to gravity, ρ, ν, β and κ are the density, kinematic viscosity, volumetric expansion coefficient and thermal diffusivity of fluid, respectively.

The appropriate initial and boundary conditions are as follows,

$$U_R=U_\Phi=U_Z=0,\ T=T_a,\ \text{at all } R,\ \Phi,\ Z \text{ and } t<0 \tag{6}$$

and at $t \geq 0$,

$$\left.\begin{aligned} U_R=U_\Phi=U_Z=0,\ \frac{\partial T}{\partial R}=0,\ \text{on } R=R_c,\ 0\leq\Phi\leq 2\pi,\ 0\leq Z\leq H;\\ U_R=U_\Phi=0,\ U_Z=W_0,\ T=T_0,\ \text{on } 0\leq R\leq R_0,\ 0\leq\Phi\leq 2\pi,\ Z=0;\\ U_R=U_\Phi=U_Z=0,\ \frac{\partial T}{\partial Z}=0,\ \text{on } R_0<R\leq R_c,\ 0\leq\Phi\leq 2\pi,\ Z=0;\\ \frac{\partial U_R}{\partial Z}=\frac{\partial U_\Phi}{\partial Z}=\frac{\partial U_Z}{\partial Z}=\frac{\partial T}{\partial Z}=0,\ \text{on } 0\leq R\leq R_c,\ 0\leq\Phi\leq 2\pi,\ Z=H. \end{aligned}\right\} \tag{7}$$

These variables can be made dimensionless by their respective scales as follows,

$$\left.\begin{aligned} r=\frac{R}{R_0},\quad z=\frac{Z}{R_0},\quad u_r=\frac{U_R}{W_0},\quad u_z=\frac{U_Z}{W_0},\quad u_\varphi=\frac{U_\Phi}{W_0},\\ \tau=\frac{t}{R_0/W_0},\quad p=\frac{P}{\rho W_0^2},\quad \theta=\frac{T-T_a}{T_a-T_0}, \end{aligned}\right\} \tag{8}$$

where r and z are the dimensionless coordinates, u_r, u_z and u_φ are the dimensionless velocity components in the r, z and φ directions, φ (in radiant) is itself dimensionless, τ, p and θ are the dimensionless time, pressure and temperature, respectively.

Re, Fr and Pr are the Reynolds, Froude and Prandtl numbers, defined as follows,

$$\mathrm{Re}=\frac{W_0 R_0}{\nu} \tag{9}$$

$$Fr=\frac{W_0}{\sqrt{gR_0(\rho_0-\rho_a)/\rho_a}}=\frac{W_0}{\sqrt{g\beta R_0(T_a-T_0)}} \tag{10}$$

$$Pr=\frac{\nu}{\kappa} \tag{11}$$

where ρ_0 and ρ_a are the densities of the jet fluid and the ambient fluid at the source, respectively. For fountains resulted from the temperature difference between the jet and ambient fluid, Fr can also be calculated with the temperature difference using the Oberbeck-Boussinesq approximation as the second expression in Eqn. (10), which requires the density ratio of $(\rho_0-\rho_a)/\rho_a$ to be significantly less than unity.

The dimensionless confinement size parameter of the cylindrical container, λ, is non-dimensionalized by R_0 as follows,

$$\lambda=\frac{R_c}{R_0}. \tag{12}$$

The above governing equations are discretized using the finite volume method and solved by the SIMPLE algorithm. The 2nd-order central difference schemes and 3rd-order QUICK scheme are used for the viscous diffusive terms and the advective terms, respectively. For the time integration of the advective terms and the diffusive terms, the 2nd-order Adams-Bashforth and Crank-Nicolson

schemes are used. The PRESTO scheme is used for the pressure gradient. All DNS runs were carried out using ANSYS Fluent 17.0.

There are 40 DNS runs carried out in this paper, with the key information of these runs presented in Table 1. Water was selected as the fluid in the numerical simulations, with density, kinematic viscosity and volume expansion coefficient of $\rho_a = 996.6$ kg/m^3, $\upsilon = 8.58 \times 10^{-7}$ m^2/s and $\beta = 2.76 \times 10^{-4}$ 1/K at the reference temperature of $T_a = 300$ K. The maximum temperature difference between the source and the ambient fluid ($T_a - T_0$) of all DNS runs is (300–296.602) = 3.398K, which results in a small enough density ratio to ensure that the Oberbeck-Boussinesq approximation is valid.

Non-uniform meshes were used for this study. A fine uniform mesh was used in the bottom region (below $H/2$), while for the top region (over $H/2$) a coarse and stretched mesh was used. Extensive mesh and time-step size independence tests were carried out to ensure accurate results to be obtained for the DNS runs. As an example of the tests, the comparison of the DNS results obtained with three different meshes and three different time-step sizes was made for the case of $Fr = 1.5$, Re = 200, $Pr = 7$ and $\lambda = 20$. The three meshes (coarse, basic and fine) were created by the ANSYS ICEM software. For the basic mesh of 4.06 million grids, the uniform grids of the sizes of $\Delta r = 0.067$ and $\Delta z = 0.067$, which are made dimensionless by R_0, are used in the region of $0 \le z \le 10$, while in the remaining region, the grid sizes expand at a rate of 0.5% in the vertical direction until they reach the open top boundary, along with 40 uniform grids created in the angular direction. When larger grid sizes of $\Delta r = 0.1$ and $\Delta z = 0.1$ were used in the uniform region and the grid size expansion rate is unchanged for the non-uniform region, the coarse mesh is created with 1.5 million grids. In the uniform region of the fine mesh, the grid sizes are reduced to $\Delta r = 0.05$ and $\Delta h = 0.05$, resulting in 5.2 million grids. The very small variations between the solutions with different meshes and different time-step sizes indicate that the basic mesh of 4.06 million grids with the time-step size of $\Delta\tau = 0.0076$ can produce a sufficient resolution for Re $\le$ 200. Similar mesh and time-step independence tests had also been carried out for other cases to ensure the accuracy of the numerical solutions.

3. DNS results benchmark

To ensure the DNS results are accurate, the DNS results of several typical confined weak round fountains are compared against the experimental results of approximately the same corresponding fountains, both qualitatively and quantitatively. The selected DNS runs include those of $Fr = 1.0$, 1.5, 2.0, and 3.0 at Re = 200 and $\lambda = 20$ (*i.e.*, Runs 14, 22, 30 and 35), and Re = 100 and 500 at $Fr = 1.5$ and $\lambda = 20$ (*i.e.*, Runs 21 and 23). The experiments chosen for the DNS benchmark are those of $Fr = 1.0$, 1.5, 2.0 and 3.0 at Re = 204 and $\lambda = 27.9$, and Re = 102 and 511 at $Fr = 1.5$ and $\lambda = 27.9$ with each experiment corresponding to the closest to its counterpart of the DNS run.

The details of the experimental system, setup, and methods were described in our recent experimental study on confined turbulent round fountain [22, 23], and the key data of these experiments are presented in Table 2.

In the experiments, saline water of various densities was ejected upward into a cylindrical container with quiescent tap water at specific constant flow rates, to form the confined round fountains. The inner diameter of the cylindrical Perspex-sided test tank is 0.39 m, with a nozzle of diameter 0.014 m on the bottom center, resulting in the dimensionless confinement size $\lambda = 27.9$. Since the fluid for the experiments is water, Pr is fixed as $Pr = 7$. By using flow visualization technique, the transient behavior of confined fountains was recorded by a system of two Photron FASTCAM Mini UX100 High-Speed Cameras and a SONY HDR-PJ810 video camera.

As will be detailed in § 4.1.1, the evolution of the flow behavior of a typical confined weak round fountain consists of five major distinct development stages, *i.e.*, the formation of the fountain flow in the ambient, the intrusion flow on the bottom of the container, the wall fountain flow on the sidewall, the reversed flow, and the density stratification. In Fig. 1, the images of the density field from the experiment for the confined weak round fountain of $Fr = 1.5$, Re = 204, $Pr = 7$ and $\lambda = 27.9$ and the contours of the temperature field from the DNS for the corresponding confined weak round fountain of $Fr = 1.5$, Re = 200, $Pr = 7$ and $\lambda = 20$ are presented for the stages of the intrusion flow, the wall fountain flow and the stratification, respectively. The results demonstrate that the experimental

Table 1
Key data for the DNS runs (Note: $h = H/R_0$).

Runs	***Fr***	**Re**	$\lambda \times h$	**Grids** (million)
1, 2	0.25	100, 200	20 × 20	4.06
3, 4, 5, 6	0.5	10, 50, 100, 200	20 × 20	4.06
7, 8	0.5	500, 800	20 × 12	5.88
9, 10, 11, 12, 13, 14	1.0	5, 10, 20, 50, 100, 200	20 × 20	4.06
15, 16	1.0	500, 800	20 × 12	5.88
17, 18	1.25	100, 200	20 × 20	4.06
19, 20, 21, 22	1.5	10, 50, 100, 200	20 × 20	4.06
23, 24	1.5	500, 800	20 × 12	5.88
25, 26	1.75	100, 200	20 × 20	4.06
27, 28, 29, 30	2.0	10, 50, 100, 200	20 × 20	4.06
31	2.0	800	20 × 12	5.88
32, 33	2.5	100, 200	20 × 20	4.06
34, 35	3.0	100, 200	20 × 20	4.06
36	1.0	200	10 × 30	3.84
37	1.0	200	15 × 30	5.78
38	1.0	200	25 × 20	4.07
39	1.0	200	30 × 20	4.89
40	1.0	200	35 × 20	5.70

Table 2
Key data of the experiments and the corresponding DNS runs.

Run	Fr	Re	R_0 (m)	W_0 (m/s)	ρ_0 (kg/m^3)	ρ_a (kg/m^3)	DNS run
1	1	204	0.007	0.0271	996.5	1007.6	14
2	1.5	102	0.007	0.0135	996.5	997.7	21
3	1.5	204	0.007	0.0271	996.5	1001.3	22
4	1.5	511	0.007	0.0677	996.6	1026.1	23
5	2	204	0.007	0.0271	996.5	999.3	30
6	3	204	0.007	0.0271	996.6	997.8	35

results and the DNS results are qualitatively in good agreement, as the DNS results captures the major features of the flow behavior with sufficient accuracy.

The quantitative comparison between the numerical and experimental results of the time series of the penetration height of the fountains and the intrusion front was also made and presented in Ref. [22] (due to the limit of figures the figures showing these results are not presented here). It was found that the DNS results are quantitatively in good agreement with the experimental results as well, although it is also noted that there are some noticeable quantitative differences presented in the results with the possible factors contributed to the differences discussed by Mahmud and his co-workers [24,25].

Nevertheless, all the benchmark results clearly show that the code used for the DNS runs is able to provide satisfactorily accurate and reliable numerical results which capture all the major features of the bulk behavior of confined round fountains in homogeneous ambient.

4. Results and discussions

4.1. Qualitative observations

4.1.1. Evolution of a typical confined weak round fountain flow

A series of snapshots of the transient temperature contours of the fountain of $Fr = 0.5$, $\mathrm{Re} = 200$, $Pr = 7$ and $\lambda = 20$ are presented in Fig. 2, which provide an overview of the evolution of a typical confined weak round fountain. After the formation of the fountain flow, the development of a typical confined weak round fountain can be divided into another four stages, *i.e.*, the intrusion flow, the wall fountain on the sidewall, the reversed flow, and the stratification.

When the fountain and intrusion flow are initially formed, the influence of the confinement is negligible, resulting in the essentially same behavior as that of its counterpart of the free round fountain, which has been illustrated in detail by Lin & Armfield [11]. Thus the description of the behavior in this period is omitted here. With the weak momentum flux at the source, the downflow of the fountain spreads outward along the bottom as shown in Fig. 2(a)–(c), behaving as a radial gravity current. The evolution of the radial intrusion flow experiences several regimes, *i.e.*, the 'wall-jet' (W-J), the 'buoyancy-inertial' (B–I), and the 'buoyancy-viscosity' (B–V) regimes in terms of the dominant governing forces. A detailed discussion of the intrusion flow will be presented in § 4.2.1.

A secondary wall fountain flow is created after the intrusion impinges with the sidewall as shown in Fig. 2(d)–(f), where the denser flow moves upward on the sidewall to reach a finite height and then falls down due to the negative buoyancy. The fountain behavior will be further studied in § 4.2.2. A flow reversal moving from the sidewall to the fountain is subsequently created due to the stagnation pressure from the sidewall, resulting in a two-layer structure as presented in Fig. 2(g)–(i). The thickness of the bottom denser fluid layer increases due to the interaction between the reversed flow and the intrusion, the fountain flow and the ambient fluid. The interaction is strengthened with the reversed flow approaching the fountain core. Subsequently, a collision of the intrusion flows from both sidewalls occurs at the center region of the container, pushing the ejected fountain flow from the source to a higher height, which subsequently falls down due to the negative buoyancy as shown in Fig. 2(k). With the continuous supply of the fountain flow from the source, a thermal stratification is eventually created, with the fountain flow submerged in the stratified fluid in the long run as shown in Fig. 2(l). After that filling and thermal conduction dominate the development of the thermal stratification.

4.1.2. The influence of Re, Fr, and λ

Fig. 3 presents the snapshots of the temperature contours of the fountains of $Fr = 1.0$, $Fr = 1.5$ and $Fr = 2.0$ with $\mathrm{Re} = 200$, $Pr = 7$ and $\lambda = 20$ at different time instants to illustrate the influence of Fr on the behavior of confined weak round fountains. When Fr increases, it is seen that it will take longer for the intrusion front to impinge with the sidewall and for the wall fountain flow to reach its maximum height, as shown in the first and second rows. Meanwhile, the intrusion thickness and the wall fountain's maximum penetration height increase when Fr increases. The reversed flow and thermal stratification shown in the next two rows indicate a stronger interaction among the reversed flow, intrusion and ambient fluid with increasing Fr, which results in a longer time for the reversed flows from both sidewalls to collide at the center region, but a shorter time for the thermal stratified surface to reach the same height. For a certain thickness of thermal stratification, as shown in the last row of Fig. 3, the difference between the temperatures at the top and the bottom indicates the strength of the stratification. With the dimensionless temperature of -1 and 0 represented by color of blue and red, the stratification is found to be weaker with increasing Fr. In the long run, the increase of Fr changes the behavior of the fountain and its secondary flows from symmetric (at $Fr = 1.0$) to asymmetric (at $Fr > 1.0$), as can be seen Fig. 3.

The influence of Re on the fountains with $Fr = 1.0$, $Pr = 7$ and $\lambda = 20$ is presented in Fig. 4. It is seen that with the increase of Re the

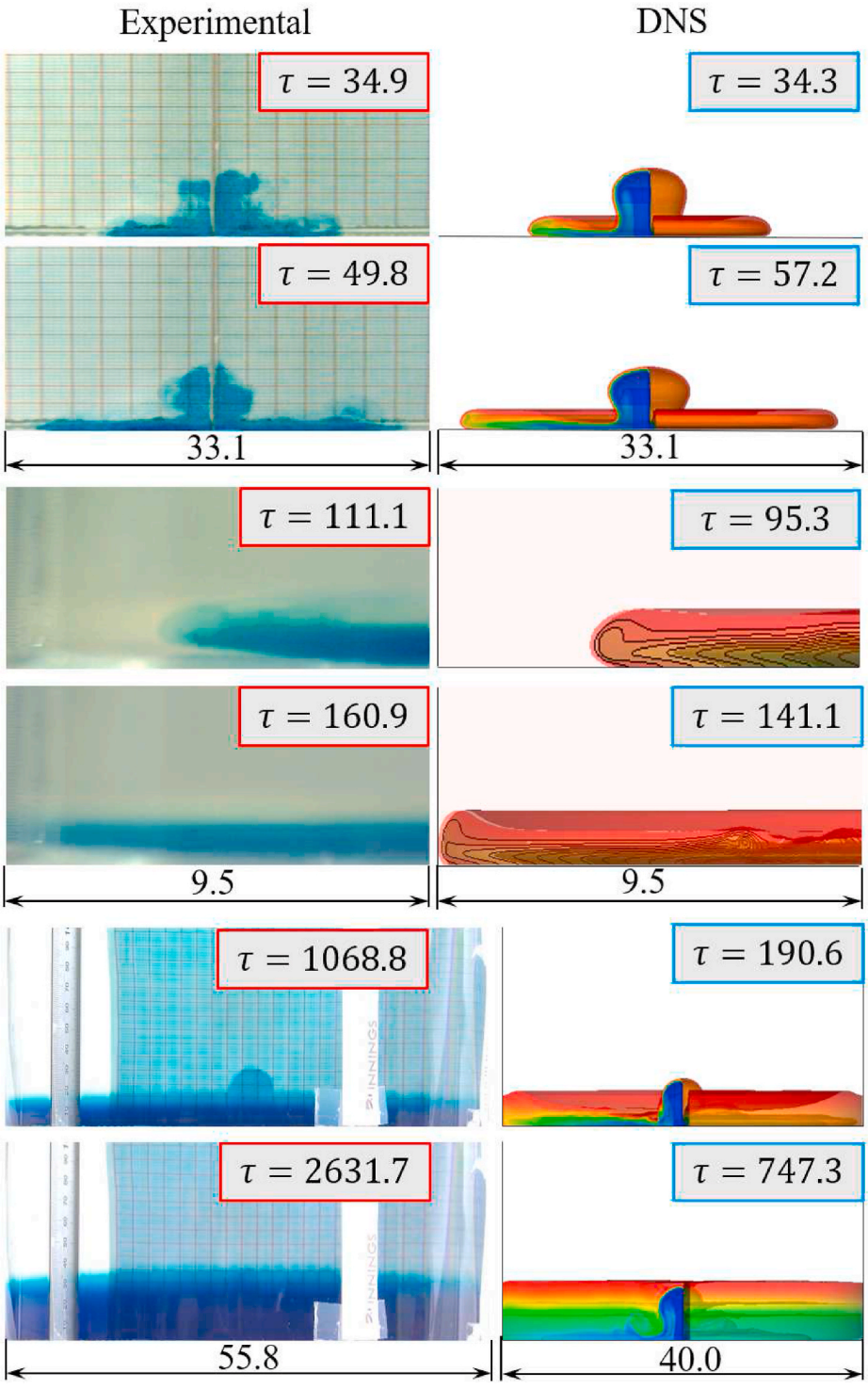

Fig. 1. The comparison between the images of the density field from the experiment for the confined weak round fountain of $Fr = 1.5$, Re = 204, $Pr = 7$ and $\lambda = 27.9$ and the contours of the temperature field from the DNS run for the corresponding confined weak round fountain of $Fr = 1.5$, Re = 200, $Pr = 7$ and $\lambda = 20$ during the intrusion flow stage (rows 1 and 2); during the wall fountain flow stage (rows 3 and 4); and during the stratification stage (rows 5 and 6), respectively.

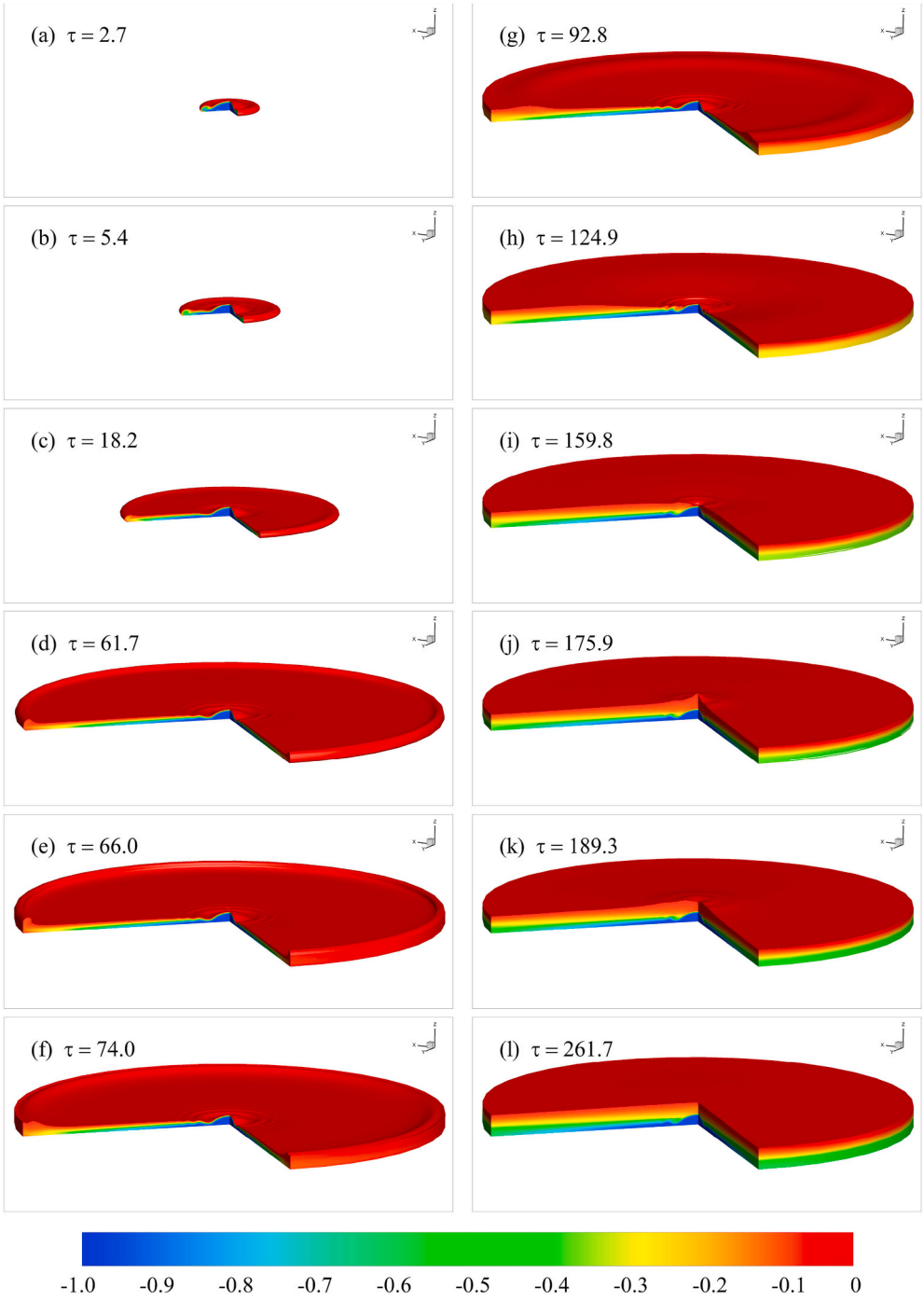

Fig. 2. The evolution of the temperature contours of the round fountain with $Fr = 0.5$, $\mathrm{Re} = 200$, $Pr = 7$ and $\lambda = 20$ over the duration of $2.7 \leq \tau \leq 261.7$.

thickness of the intrusion, the wall fountain maximum penetration height, and the stratification height all become smaller, but the stratification turns stronger, *i.e.*, the temperature difference between the top and bottom becomes larger. From the first row, it is seen that the intrusion speed becomes larger when Re increases but the time for the wall fountain to reach the maximum height is reduced, as shown in the second row. However, it takes longer to form the stratification with a larger Re as shown in the last row. The interaction between the fountain flow and its secondary flows becomes more significant when Re becomes larger, resulting in the enlargement of the region of the fountain core (the blue part at the region center). This is because a stratified structure with a denser fluid (blue) surrounding the fountain is formed, which will reduce the stability of the fountain flow. Hence, a very weak asymmetric behavior

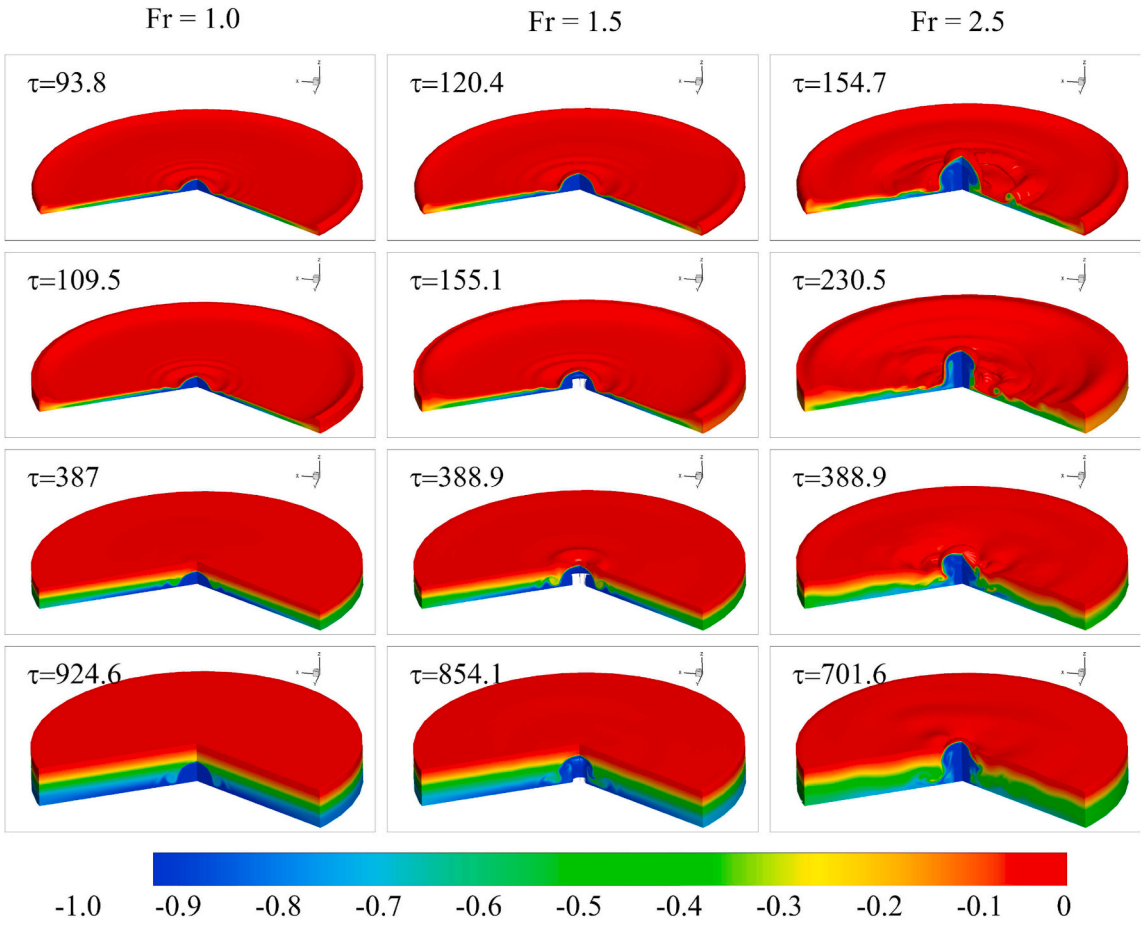

Fig. 3. The snapshots of the temperature contours of the fountains with different *Fr* values, all with Re = 200, *Pr* = 7 and $\lambda = 20$. The left, middle and right columns are for *Fr* = 1.0, *Fr* = 1.5 and *Fr* = 2.5, respectively.

appears for the intrusion near the fountain core for the fountain with Re = 800. It should be noted that no falling of the wall fountain is observed for the fountains with Re $\leq$ 20, although the results are not presented here.

When λ increases, it is found from the results that the wall fountain reaches a higher maximum height, and it takes longer to establish a weaker stratification in the container, as shown in Fig. 5.

4.2. Quantitative observation

4.2.1. Intrusion

The time series of the intrusion front for the confined round fountains over $0.25 \leq Fr \leq 3.0$, $5 \leq \mathrm{Re} \leq 800$, and $10 \leq \lambda \leq 35$ at $Pr = 7$ are presented in Fig. 6 (left column). The intrusion front is determined as the *r*-location where the temperature is $T(r) = T_a - 1\%(T_a - T_0)$ within the whole cylindrical domain. The end point of the times series is defined as the characteristic time-scale for the intrusion front impinging with the sidewall, τ_w. The intrusion speed is found to increase when *Fr* decreases or when Re increases, as shown in Fig. 6(a) and 6(b), respectively. Only the early stages of the intrusion passages overlap for fountains with Re $\geq$ 500, while a larger intrusion velocity is observed for the cases with larger Re at the later stages. The influence of λ is presented in Fig. 6(c), which shows that the λ effect becomes significant only in the region close to the sidewall. All these are consistent with the qualitative observations described above, indicating that the effect of thermal conduction becomes more significant with a larger *Fr* or a smaller Re.

For practical examples such as the reverse cycle air-conditioning systems in the building and the leakage of hazardous gas in a limited space, τ_w represents the time taken for the cold/hot air or hazardous gas to reach the sidewall, which is important for evaluating the performance of the air-conditioning systems and guiding the relief. To illustrate the influence of the governing parameters on τ_w, τ_w is also plotted against *Fr*, Re and λ respectively in Fig. 6 (right column). From Fig. 6(d), combined with the behavior of the wall fountain, the stratification and the entrainment with variable *Fr* studied in § 4.2.2, § 4.2.3 and § 4.2.4, two critical values, around *Fr* = 1.0 and *Fr* = 2.0, are identified to distinguish the influence of *Fr* into three ranges, with three different correlations are determined as follows:

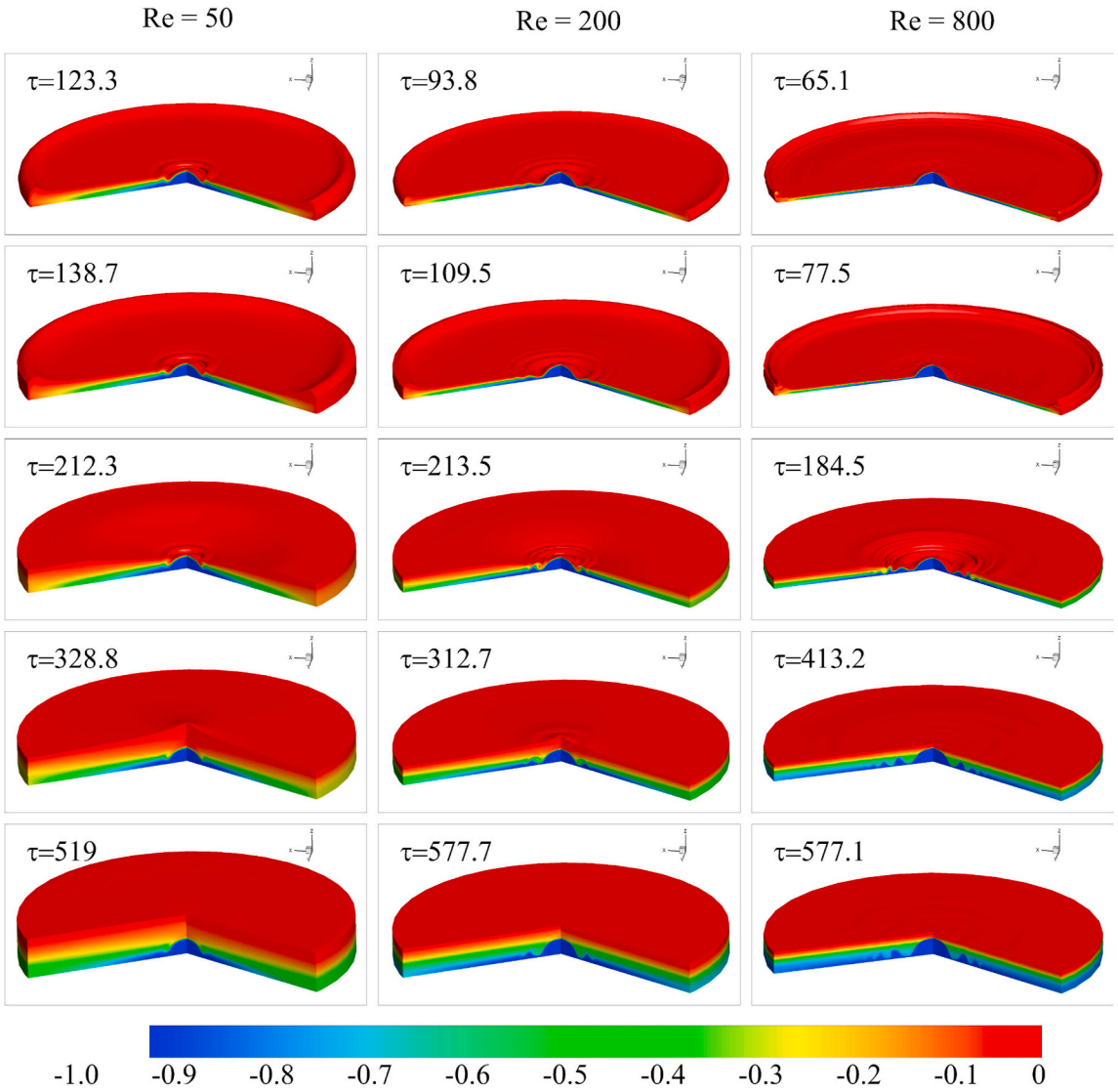

Fig. 4. The snapshots of the temperature contours of the fountains with different Re values, all with $Fr = 1.0$, $Pr = 7$ and $\lambda = 20$. The left, middle and right columns are for Re = 50, Re = 200 and Re = 800, respectively.

$$\tau_w = \begin{cases} 94Fr^{0.61} - 0.26, & 0.25 \le Fr \le 1.0, \\ 50.8Fr + 43.7, & 1.0 \le Fr \le 1.75, \\ 35.2Fr + 66.1, & 2.0 \le Fr \le 3.0, \end{cases} \tag{13}$$

with $R^2 = 1$, 0.998 and 0.999, respectively. It should be noted that $Fr = 1$ and 2 are only the approximate critical values. To determine the exact Fr critical values, many more numerical runs with different Fr values should be carried out. It should also be noted that the values obtained for the exponents and the constants in the above equation and the subsequent equations are indicative only as many more numerical runs for different Fr values and other governing parameters (Re and λ) should be carried out to determine their values more accurately. Fig. 6(e) demonstrates the influence of Re on τ_w. Similarly, two ranges of Re, *i.e.*, $5 \le \mathrm{Re} \le 200$ and $200 \le \mathrm{Re} \le 800$ are determined, with the correlations between τ_w and Re can be quantified as follows:

$$\tau_w = \begin{cases} 217.4\mathrm{Re}^{-0.159} + 3.8, & 5 \le \mathrm{Re} \le 200, \\ 377.8\mathrm{Re}^{-0.263} + 0.1, & 200 \le \mathrm{Re} \le 800, \end{cases} \tag{14}$$

with $R^2 = 0.985$ and 1 respectively. Similarly, Re = 200 is only the approximate critical value and the exact Re critical value should be determined with many more numerical runs with different Re values. From the results shown in Fig. 6(f), the following power law correlation between τ_w and λ over $10 \le \lambda \le 35$ is obtained,

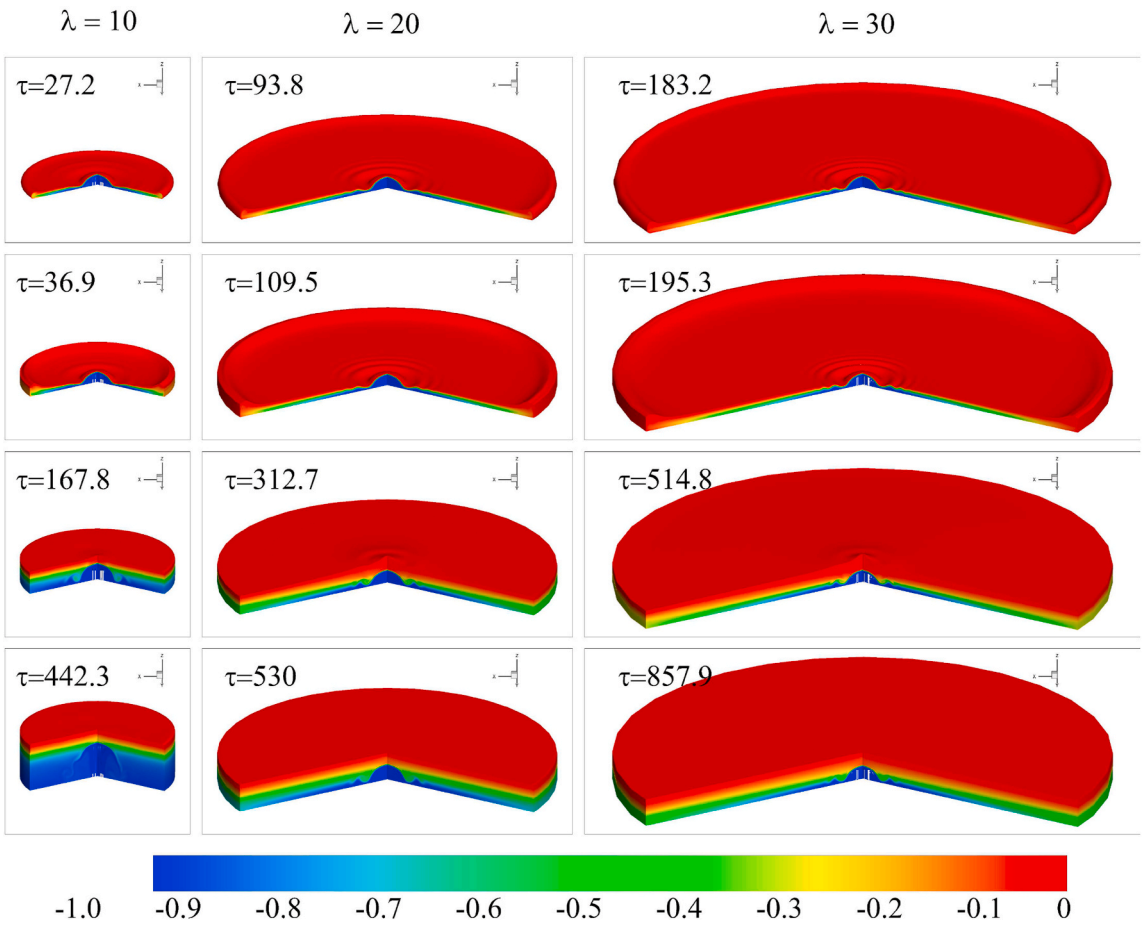

Fig. 5. The snapshots of the temperature contours of the fountains with different λ values, all with $Fr = 1.0$, Re $= 200$ and $Pr = 7$. The left, middle and right columns are for $\lambda = 10$, 20 and 30, respectively.

$$\tau_w = 0.5\lambda^{1.73} + 1.7, \tag{15}$$

with $R^2 = 1$.

4.2.2. Wall fountain

After the impingement of intrusion with the sidewall, the flow is turned upward and moves on the sidewall up to a certain height due to the negative buoyancy before it falls down, forming a wall fountain flow. The behavior of wall fountain mainly depends on Re. There is no falling down observed for the wall fountain with Re ≤ 20, while the wall fountain slumps down after reaching its maximum penetration height for $50 \leq$ Re ≤ 800. However, no rolling down behavior similar to the counterpart of the 'plume filling box' flow [26] is found for the wall fountain of the confined fountains considered here.

The time series of the wall fountain front in the region close to the sidewall are plotted in Fig. 7 (top row) over $0.25 \leq Fr \leq 3.0$, $5 \leq$ Re ≤ 800 and $10 \leq \lambda \leq 35$, all at $Pr = 7$, with the wall fountain front defined as the vertical location in the region close to the sidewall where the temperature is $T(y) = T_a - 1\%(T_a - T_0)$. The maximum penetration height of the wall fountain, z_m (non-dimensionalized by R_0), is determined at the largest value of z in the time series, and the corresponding time, τ_m (non-dimensionalized by R_0/W_0), is determined as the time-scale for the wall fountain reaches its maximum penetration height, as shown in Fig. 7(a). In the practical situation of hazardous gas leakage, for example, z_m indicates the maximum height of the region close to the sidewall to be initially influenced, which is necessary information for the evacuation and relief.

For $Fr \leq 1.75$, z_m is found to increase with Fr, along with a larger corresponding τ_m, while this conclusion is not valid for $Fr \geq 2.0$, due to the stronger convection as shown in Fig. 3. Similarly, with the increase of λ, z_m and τ_m increase. The increase of Re results in a smaller z_m and also shortens the time for the wall fountain to reach its maximum height.

The middle and bottom rows in Fig. 7 demonstrate the quantitative influence of Fr, Re and λ on τ_m and z_m, respectively. From Fig. 7 (d), $Fr = 1.0$ and $Fr = 2.0$ are determined as the approximate critical values to distinguish the influence of Fr into three different ranges, with the following correlations obtained between τ_m and Fr,

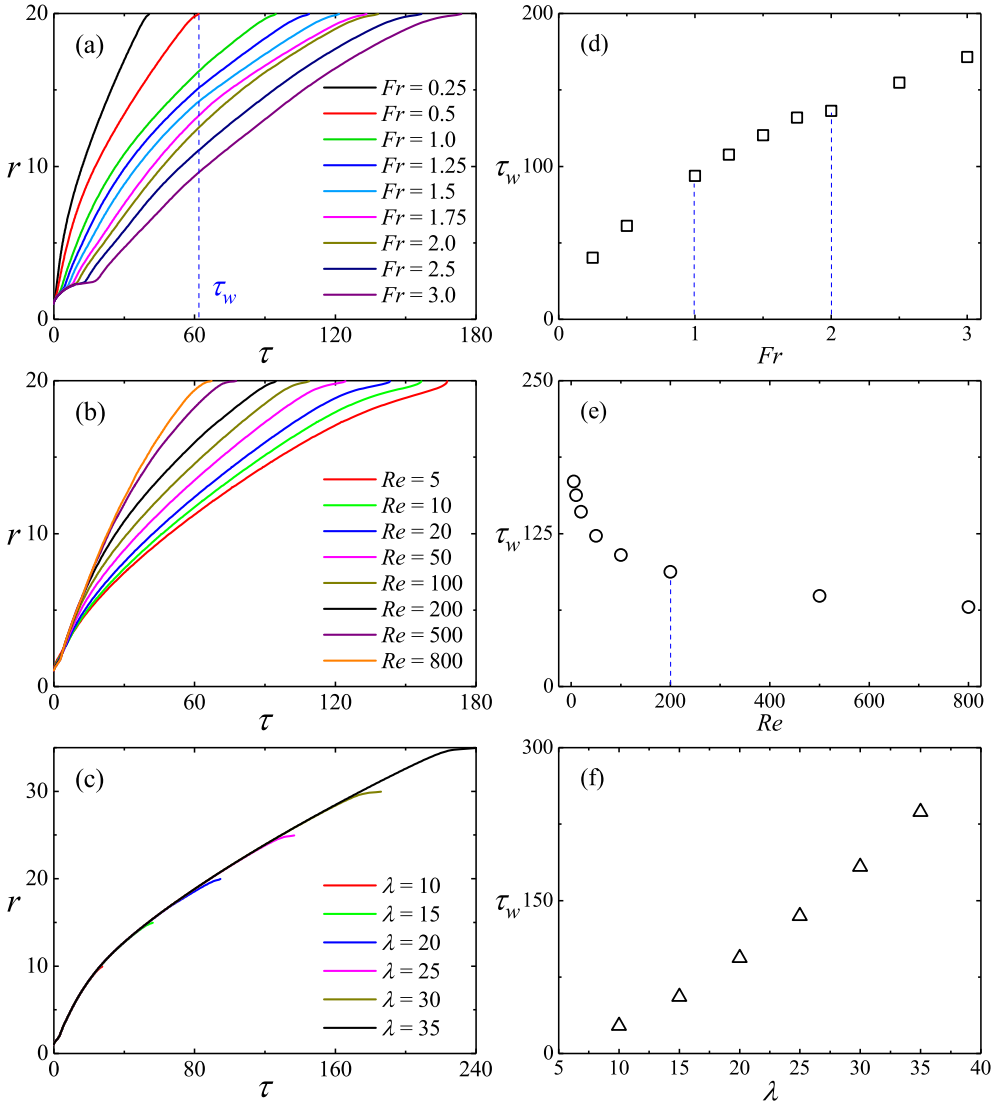

Fig. 6. The time series of the passage of the intrusion front (left column) and τ_w (right column) for confined weak round fountains with (a) and (d) $0.1 \le Fr \le 3.0$, all at Re = 200, $Pr = 7$, and $\lambda = 20$; (b) and (e) $5 \le \mathrm{Re} \le 800$, all at $Fr = 1.0$, $Pr = 7$, and $\lambda = 20$; and (c) and (f) $10 \le \lambda \le 35$, all at $Fr = 1.0$, Re = 200, and $Pr = 7$.

$$\tau_m = \begin{cases} 109.4Fr^{0.68} - 0.21, & 0.25 \le Fr \le 1.0, \\ 92.1Fr + 20.1, & 1.0 \le Fr \le 1.75, \end{cases} \tag{16}$$

with $R^2 = 1$ and 0.998, respectively. There is no clear correlation obtained for the range of $2.0 \le Fr \le 3.0$, due to the small number of points.

No τ_m is obtained for the fountains with $\mathrm{Re} \le 20$ since there is no slumping down behavior for their wall fountain flows. For the fountains with $50 \le \mathrm{Re} \le 800$, the influence of Re is distinguished into two ranges approximately by Re = 200, as shown in Fig. 7(e), and the following two power-law correlations are obtained,

$$\tau_m = \begin{cases} 270.9\mathrm{Re}^{-0.17} - 1.47, & 50 \le \mathrm{Re} \le 200, \\ 410.5\mathrm{Re}^{-0.25} + 0.45, & 200 \le \mathrm{Re} \le 800, \end{cases} \tag{17}$$

with $R^2 = 0.99$ and 1, respectively.

The results shown in Fig. 7(f) indicate a power-law correlation for the influence of λ on τ_m, which is quantified with the numerical results as follows,

$$\tau_m = 1.1\lambda^{1.53} + 1.16, \tag{18}$$

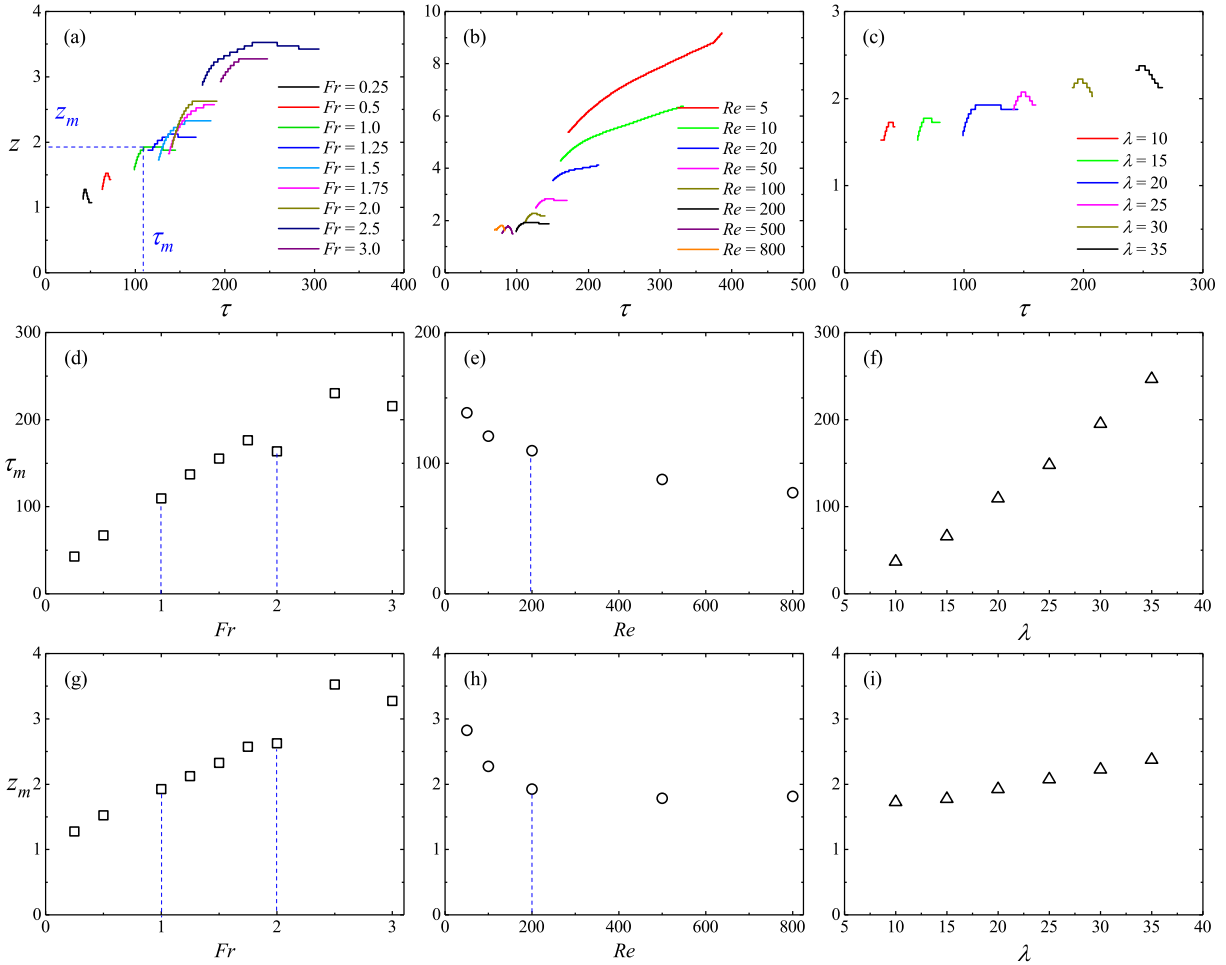

Fig. 7. The time series of the wall fountain front (top row), τ_m (middle row), and z_m (bottom row) for fountains with (a), (d), (g) Re = 200, $Pr = 7$, $\lambda = 20$, and $0.25 \leq Fr \leq 3.0$; (b), (e), (h) $Fr = 1.0$, $Pr = 7$, $\lambda = 20$, and $5 \leq \mathrm{Re} \leq 800$; and (c), (f), (i) $Fr = 1.0$, Re = 200, $Pr = 7$, and $10 \leq \lambda \leq 35$.

with $R^2 = 0.999$.

From Fig. 7(g), it is seen that the influence of Fr on z_m is again divided into three ranges approximately by $Fr = 1.0$ and $Fr = 2.0$, with following correlations obtained over $0.25 \leq Fr \leq 1.0$ and $1.0 \leq Fr \leq 1.75$,

$$z_m = \begin{cases} 1.92Fr^{0.3} - 0.01, & 0.25 \leq Fr \leq 1.0, \\ 0.86Fr + 1.06, & 1.0 \leq Fr \leq 1.75, \end{cases} \tag{19}$$

with $R^2 = 0.995$ and 0.998 respectively, but again there is no clear correlation over $2.0 \leq Fr \leq 3.0$ due to the same reason as mentioned above. Fig. 7(h) shows the influence of Re on z_m. For $\mathrm{Re} \geq 200$, the effect of Re on z_m is minimal, while for $50 \leq \mathrm{Re} \leq 200$, the following correlation is obtained,

$$z_m = 8.38\mathrm{Re}^{-0.28} - 0.03, \tag{20}$$

with $R^2 = 0.995$. The influence of λ on z_m presented in Fig. 7(i) can be quantified by the following linear correlation,

$$z_m = 0.027\lambda + 1.41, \tag{21}$$

with $R^2 = 0.985$.

4.2.3. Stratification

With the continuous ejection of the fountain fluid, a time-dependent thermally stratified structure is formed in the container. The stratification height is defined as the z-location at which the temperature is $T(z) = T_a - 1\%(T_a - T_0)$ within the whole container, which is the interface between the stratified fluid created by the filling of cold fluid through the fountain flow and the ambient fluid. The time series of the maximum, minimum and averaged stratification heights presented in Fig. 8 (left column) are used to demonstrate the

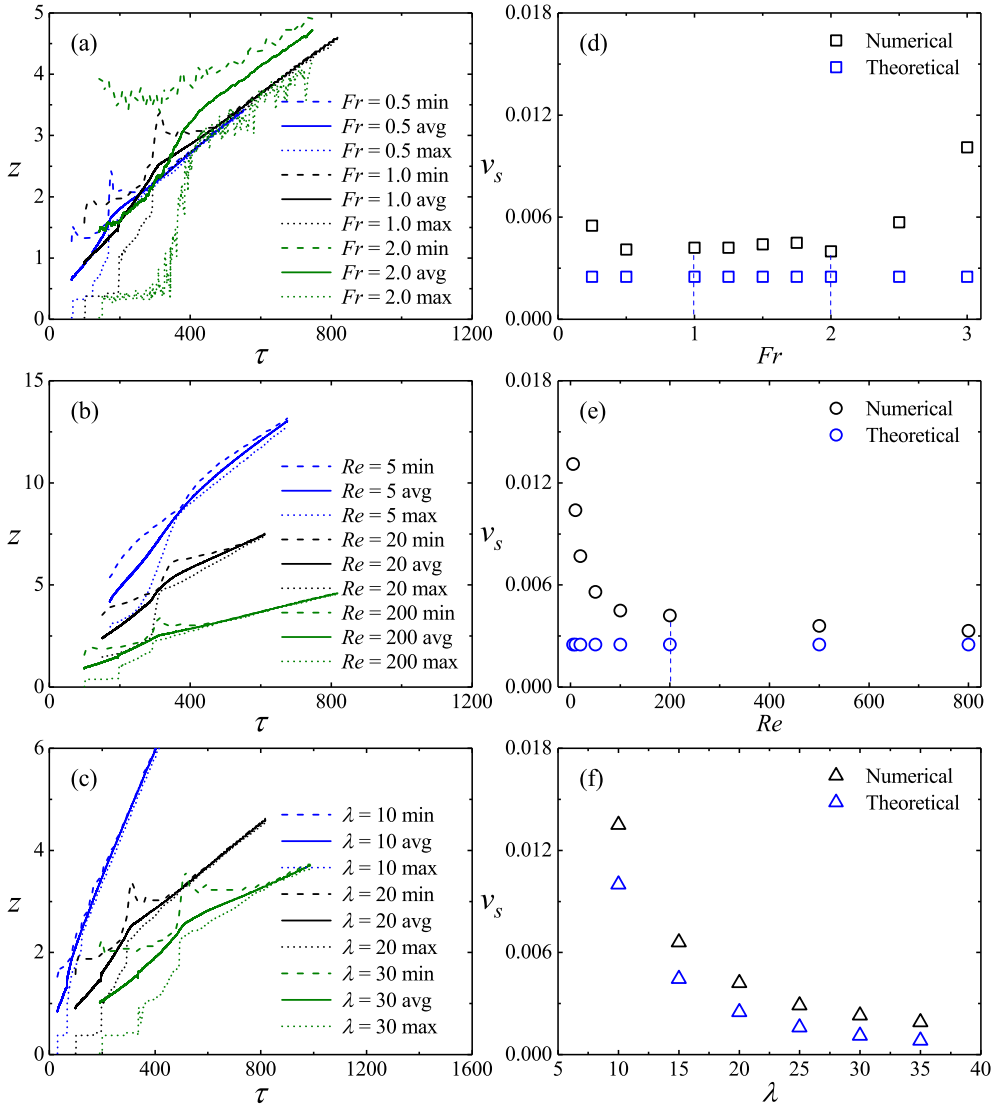

Fig. 8. The time series of the maximum, minimum and average stratification heights (left column) and v_s (right column) for fountains with (a) and (d) varying *Fr*, all at Re = 200, $Pr = 7$, $\lambda = 20$; (b) and (e) varying Re, all at $Fr = 1.0$, $Pr = 7$, $\lambda = 20$; and (c) and (f) varying λ, all at $Fr = 1.0$, Re = 200, $Pr = 7$.

influence of *Fr*, Re, and λ. The time series of the stratification height in the figure starts from the instant when the intrusion impinges with the sidewall until a quasi-steady stratification is formed when the differences among the maximum, averaged and minimum heights become small enough or overlap. At the initial stage, the differences among these height time series are significant. This is because convection and mixing play dominant roles in the flow development, which is mainly resulted from the interactions among the fountain flow, its secondary flows (wall fountain and reversed flow) and the ambient fluid. In the long run, the three time series follow the same trend and converge together, indicating that thermal conduction and filling become the dominant mechanism at the later stratification stage.

Fig. 8(a) shows that the extents of differences among the time series of the stratification height become larger when *Fr* increases, and the time for the formation of the quasi-steady stratification also increases. However, the results in Fig. 8(b) indicate that the increase of Re results in smaller extents of the differences among the time series, a shorter time for the stratification to reach steady, and a smaller development rate of the quasi-steady stratification, which is approximately represented by the slope of the averaged time series of the height, due to the influence of thermal conduction. It is also found that the extents of the differences among the time series become larger when λ increases, as shown in Fig. 8(c), which is due to the higher penetration height of the wall fountain.

While the development rate of the stratification, v_s, which is $dz/d\tau$, can be approximately obtained through the slope of the averaged time series after the quasi-steady stratification is formed, its counterpart for a purely filling flow in a cylindrical container can be calculated by $v_s = 1/\lambda^2$ based on the conservation of mass. Fig. 8 (right column) presents the development rate of the averaged

stratification of the confined fountains and that of the purely filling flow to illustrate the influence of Fr, Re and λ on v_s for confined fountains. Again, $Fr = 1.0$ and $Fr = 2.0$ are determined as the approximate critical values to distinguish the influence of Fr into three ranges, as shown in Fig. 8(d). For $0.25 \leq Fr < 1.0$, the increase of Fr results in a declining v_s. But v_s remains almost constant for $1.0 \leq Fr \leq 2.0$, whereas the further increase of Fr causes v_s to increases noticeably over $2.0 < Fr \leq 3.0$. Fig. 8(e) illustrates the influence of Re on v_s, where the influence of Re can be distinguished into two ranges by a specific value between Re = 100 and Re = 200, with two power-law correlations obtained as follows,

$$v_s = \begin{cases} 0.09\mathrm{Re}^{-0.362}, & 5 \leq \mathrm{Re} \leq 100, \\ 0.07\mathrm{Re}^{-0.173}, & 200 \leq \mathrm{Re} \leq 800, \end{cases} \tag{22}$$

with $R^2 = 0.998$ and 1.0 respectively. With the results presented in Fig. 8(f), the following correlation is obtained between v_s and λ,

$$v_s = 0.5077Pr^{-1.574} - 0.0002, \tag{23}$$

with $R^2 = 0.998$.

4.2.4. Bulk entrainment or dilution

The bulk entrainment rate determined by $\eta = Q_E/Q_0$ is used to describe the mean dilution of the buoyancy scalar over the filling box as a whole, which is again used here to investigate the entrainment/dilution behavior of the filling flow with weak round fountains. Q_E is the bulk entrainment by the fountain and Q_0 is the source volume flux. For a confined round fountain, the source volume flux is $Q_0 = \pi R_0^2 W_0$, whereas the bulk entrainment Q_E is calculated by $Q_E = Q_s - Q_0$, where Q_s is the volume flux of the stratified fluid, which is calculated by integrating the volume under the thermal stratified surface.

The entrainment rates η for the confined round fountains over $0.25 \leq Fr \leq 3.0$, $5 \leq \mathrm{Re} \leq 800$, and $10 \leq \lambda \leq 35$ at $Pr = 7$ are calculated and plotted against τ as shown in Fig. 9 (top row) to demonstrate the influence of these governing parameters. The time series of the entrainment rate starts from the formation stage of the fountain until the formation of the quasi-steady stratification, performing a saddle-like profile with two peak points. The first peak point, also the maximum value of η in the time series, is denoted as η_m, and the corresponding time, τ_e (non-dimensionalized by R_0/W_0), is determined as the time-scale for the filling flow to reach its maximum entrainment rate, as shown in Fig. 9(a). The middle and bottom rows in Fig. 9 demonstrate the influence of Fr, Re and λ on τ_e and η_m, respectively.

The results show that the entrainment rate time series can be approximately distinguished into three stages with the two peak points. In the first stage, the entrainment rate increases monotonically with time until reaching the first peak point. This stage corresponds to the period of the intrusion development, where the ambient fluid is mainly engulfed by the eddy over the intrusion head. With the intrusion front impinging with the sidewall and the formation of the wall fountain, the entrainment rate time series reaches its maximum value, due to the stronger convection and mixing resulted from the impingement and the subsequent wall fountain flow. This is demonstrated by comparing Fig. 9(d)–(e) with Fig. 6(d)–(e) and Fig. 7(d)-(e), in which the value of τ_e under different parameters is similar to its counterpart of τ_w and τ_m, except for the case of $Fr \geq 2.0$ due to the stronger convection.

Then the convection and the interactions among the intrusion, the reversed flow and the ambient fluid keep the entrainment rate at a relatively high value until the reversed flows from both sidewalls collide at the center region of the container, when the second peak point appears. As shown in Fig. 9 (top row), the second peak point becomes less significant with increasing Re or decreasing λ. For $Fr \leq 1.75$, the time series of entrainment rate is relative smooth with a more significant second peak point for the smaller Fr, while the profile turns considerably fluctuating for $Fr \geq 2.0$.

After the quasi-steady stratification is formed, thermal conduction becomes the main contribution to the development of the stratification, with η increasing with increasing Fr or decreasing Re as shown in the third stage of the time series of Fig. 9(a)–(b). It should be noted that thermal conduction keeps influencing the dilution process at all stages. The influence of Fr, Re and λ on η is consistent with the results presented in § 4.2.3 for the stratification rate.

τ_e is plotted against Fr, Re and λ in Fig. 9(d)–(f) respectively to illustrate the influence of the governing parameters on τ_e. Similarly, $Fr = 1.0$ and $Fr = 2.0$ are determined as the approxinate critical values to distinguish the influence of Fr into three different ranges, with the following correlations obtained from the numerical results,

$$\tau_e = \begin{cases} 102.43Fr^{0.63} - 0.17, & 0.25 \leq Fr \leq 1.0, \\ 54.46Fr + 48.28, & 1.0 \leq Fr \leq 1.75, \end{cases} \tag{24}$$

with $R^2 = 1$ and 0.999, respectively. From Fig. 9(e), a specific value between Re = 100 and Re = 200 should exist to distinguish the influence of Re into two ranges, with two power-law correlations obtained from the numerical results as follows,

$$\tau_e = \begin{cases} 223.08\mathrm{Re}^{-0.15} + 6.68, & 5 \leq \mathrm{Re} \leq 100, \\ 311.94\mathrm{Re}^{-0.21} - 1.18, & 200 \leq \mathrm{Re} \leq 800, \end{cases} \tag{25}$$

with $R^2 = 0.993$ and 0.952 respectively. With the results presented in Fig. 9(f), the following correlation is obtained from the numerical results,

$$\tau_e = 0.68\lambda^{-1.66} + 1.69, \tag{26}$$

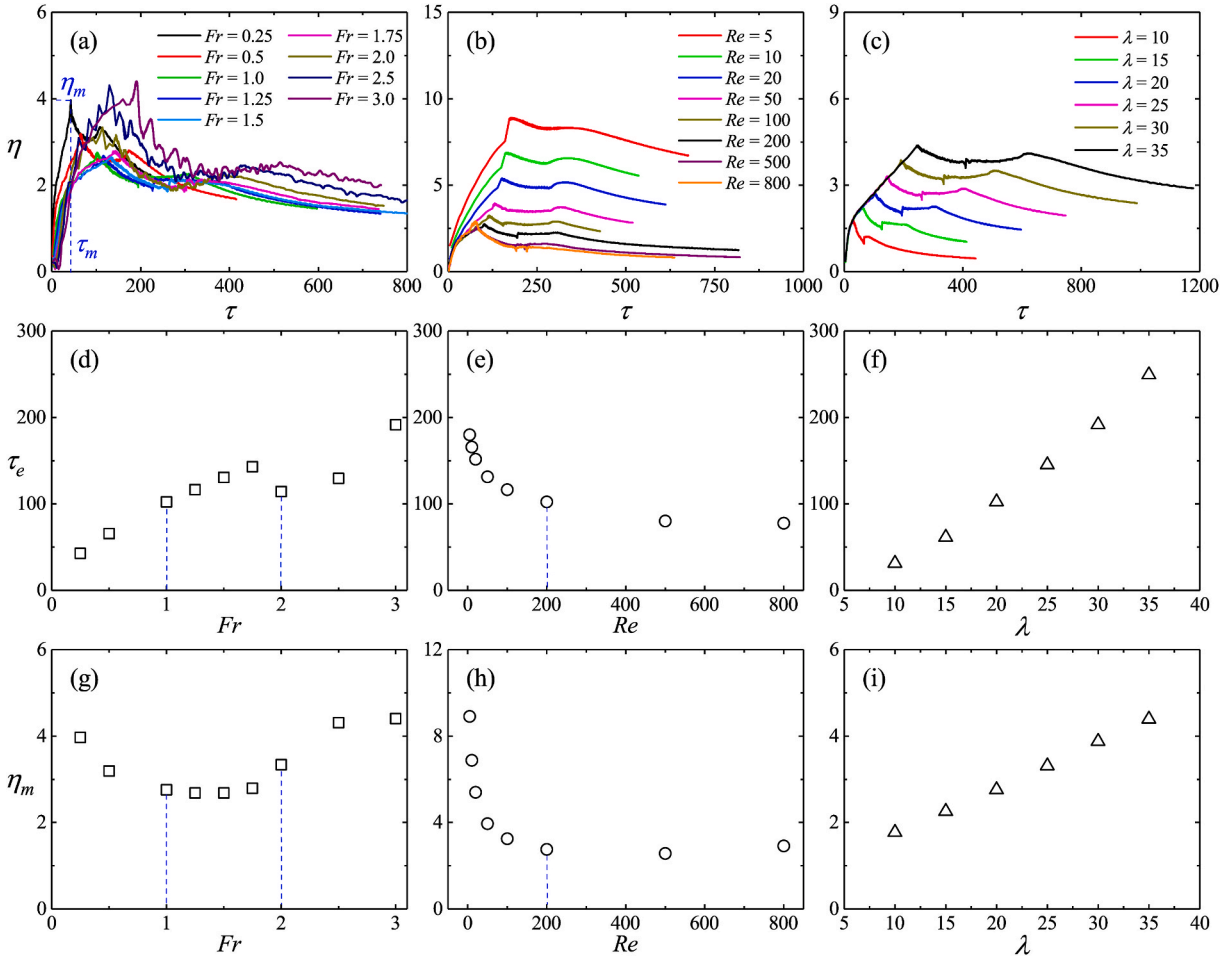

Fig. 9. The time series of the entrainment rate η (top row), τ_e (middle row), and η_m (bottom row) for fountains with (a), (d), (g) Re = 200, $Pr = 7$, $\lambda = 20$, and $0.25 \leq Fr \leq 3.0$; (b), (e), (h) $Fr = 1.0$, $Pr = 7$, $\lambda = 20$, and $5 \leq \mathrm{Re} \leq 800$; and (c), (f), (i) $Fr = 1.0$, Re = 200, $Pr = 7$, and $10 \leq \lambda \leq 35$.

with $R^2 = 0.999$.

Fig. 9(g)–(i) demonstrate the quantitative influence of Fr, Re and λ on η_m, respectively. Again, $Fr = 1.0$ and $Fr = 2.0$ are determined as the approximate critical values to distinguish the influence of Fr into three ranges, as shown in Fig. 9(g). For $0.25 \leq Fr < 1.0$, η_m decreases with the increase of Fr. However, an almost constant η_m is observed for $1.0 \leq Fr < 2.0$. After that, the further increase of Fr causes η_m to increase noticeably over $2.0 \leq Fr \leq 3.0$. Fig. 9(h) illustrates the influence of Re on η_m. For $\mathrm{Re} \geq 200$, the effect of Re on η_m is minimal, while for $5 \leq \mathrm{Re} \leq 200$, the following correlation is obtained from the numerical results,

$$\eta_m = 14.94\mathrm{Re}^{-0.32} - 0.19, \tag{27}$$

with $R^2 = 0.996$. The influence of λ on η_m presented in Fig. 9(i) can be quantified by the following linear correlation,

$$\eta_m = 0.106\lambda + 0.68, \tag{28}$$

with $R^2 = 0.999$.

5. Conclusion

For confined weak round fountains, a secondary radial intrusion flow is created with the impingement of the fountain downflow on the bottom of the container. The intrusion flow behaves as a radial gravity current. The behavior of the secondary wall fountain for the confined fountains with specific values of Fr and Re is also significantly influenced by the confinement λ. The wall fountain front on the sidewall changes from no falling to falling with the increase of λ. The maximum penetration height z_m is found to increase with λ and Fr for $Fr \leq 2.0$, whereas it decreases with increasing Re. Three stages are determined from the time series of the bulk entrainment rate. At the first stage, the entrainment rate monotonically increases due to the ambient fluid engulfed by the intrusion head. With the intrusion impinging with the sidewall and the formation of the wall fountain, the entrainment rate reaches a peak value. Subsequently, the

interactions among the intrusion, the reversed flow and the ambient fluid create convection and mixing, leading to the second stage with a relatively high entrainment rate. After the second peak, the entrainment rate gradually decreases, which is because the dominant mechanisms for the stratification development switch to filling and thermal conduction. The stratification rate v_s deceases with the increase of Re, which reduces the effect of thermal conduction. The results show that $Fr = 1.0$ and 2.0 are the critical values to distinguish the behavior of the intrusion, wall fountain and stratification. This is consistent with the existing classifications of the round fountains [1], while Re = 200 is determined as the critical value to divide the influence of Re, which also agrees well with the existing results [13].

Credit authorship contribution statement

Liqiang Dong: Conceptualization, Methodology, Investigation, Writing - original and revision draft.
Wenxian Lin: Supervision, Conceptualization, Writing - review & editing.
Mehdi Khatamifar: Methodology, Review and editing - original draft.

Declaration of competing interest

The authors declare that they have no known competing financial interests or personal relationships that could have appeared to influence the work reported in this paper.

Acknowledgment

The support from the Australian Research Council is gratefully acknowledged. Liqiang Dong would like to thank James Cook University for the JCUPRS scholarship.

References

[1] G.R. Hunt, H.C. Burridge, Fountains in industry and nature, Annu. Rev. Fluid Mech. 47 (2015) 195–220.
[2] J.-C. Chen, Studies on Gravitational Spreading Currents, Ph.D. Thesis, California Institute of Technology, 1980.
[3] P. Linden, G. Lane-Serff, D. Smeed, Emptying filling boxes: the fluid mechanics of natural ventilation, J. Fluid Mech. 212 (1990) 309–335.
[4] P. Linden, The fluid mechanics of natural ventilation, Annu. Rev. Fluid Mech. 31 (1999) 201–238.
[5] D. Bower, C. Caulfield, S.D. Fitzgerald, A.W. Woods, Transient ventilation dynamics following a change in strength of a point source of heat, J. Fluid Mech. 614 (2008) 15–37.
[6] N. Kaye, G. Hunt, Smoke filling time for a room due to a small fire: the effect of ceiling height to floor width aspect ratio, Fire Saf. J. 42 (5) (2007) 329–339.
[7] W.D. Baines, J.S. Turner, I.H. Campbell, Turbulent fountains in an open chamber, J. Fluid Mech. 212 (1990) 557–592.
[8] W.D. Baines, J.S. Turner, Turbulent buoyant convection from a source in a confined region, J. Fluid Mech. 37 (1969) 51–80.
[9] N. Williamson, N. Srinarayana, S.W. Armfield, G.D. McBain, W. Lin, Low-Reynolds-number fountain behaviour, J. Fluid Mech. 608 (2008) 297–318.
[10] J.S. Turner, Buoyant plumes and thermals, Annu. Rev. Fluid Mech. 1 (1969) 29–44.
[11] W. Lin, S. Armfield, Direct simulation of weak axisymmetric fountains in a homogeneous fluid, J. Fluid Mech. 403 (2000) 67–88.
[12] W. Lin, S. Armfield, Very weak fountains in a homogeneous fluid, Numeri. Heat Transfer A: Applications 38 (4) (2000) 377–396.
[13] W. Lin, S. Armfield, The Reynolds and Prandtl number dependence of weak fountains, Comput. Mech. 31 (2003) 379–389.
[14] N.B. Kaye, G.R. Hunt, Weak fountains, J. Fluid Mech. 558 (2006) 319–328.
[15] N. Srinarayana, N. Williamson, S.W. Armfield, W. Lin, Line fountain behavior at low-Reynolds number, Int. J. Heat Mass Tran. 53 (2010) 2065–2073.
[16] W. Baines, Entrainment by a plume or jet at a density interface, J. Fluid Mech. 68 (1975) 309–320.
[17] M. Kumagai, Turbulent buoyant convection from a source in a confined two layered region, J. Fluid Mech. 147 (1984) 105–131.
[18] S. Cardoso, A. Woods, Mixing by a turbulent plume in a confined stratified region, J. Fluid Mech. 250 (1993) 277–305.
[19] A.B. Shrinivas, G.R. Hunt, Confined turbulent entrainment across density interfaces, J. Fluid Mech. 779 (2015) 116–143.
[20] A. Debugne, G.R. Hunt, The influence of spanwise confinement on round fountains, J. Fluid Mech. 845 (2018) 263–292.
[21] N. Xue, S. Khodaparast, H. Stone, Fountain mixing in a filling box at low Reynolds numbers, Phys. Rev. Fluids 4 (2019), 024501.
[22] L. Dong, Intrusion, Wall Fountain and Stratification of Homogeneous Fluid in Confined Space Filling with Fountains, Ph.D. Thesis, James Cook University, 2019.
[23] L. Dong, W. Lin, M. Khatamifar, Experimental study on the intrusion and stratification produced by confined laminar and turbulent round fountains, Int. J. Heat Fluid Flow 89 (2021) 108785.
[24] H. Mahmud, Behavior of Multiple Transitional Round Fountains Interacting in Homogeneous and Stratified Fluids, James Cook University, 2014. PhD. thesis.
[25] H. Mahmud, W. Lin, W. Gao, S. Armfield, Y. He, Behavior of the interaction between twin transitional round fountains in a homogeneous fluid, part 2: numerical study, Int. J. Heat Mass Tran. 86 (2015) 973–991.
[26] N. Kaye, G. Hunt, Overturning in a filling box, J. Fluid Mech. 576 (2007) 297–323.